# Boosting Electrochemical Carbon Dioxide Reduction on Atomically Dispersed Nickel Catalyst

Qi Hao[1,2], Dong-Xue Liu[1], Ruiping Deng[2] and Hai-Xia Zhong[2,3]*

[1]Key Laboratory of Automobile Materials, Ministry of Education, School of Materials Science and Engineering, Jilin University, Changchun, China, [2]State Key Laboratory of Rare Earth Resource Utilization, Changchun Institute of Applied Chemistry, Chinese Academy of Sciences, Changchun, China, [3]Center for Advancing Electronics Dresden (cfaed), Faculty of Chemistry and Food Chemistry, Technische Universität Dresden, Dresden, Germany

Single-atom catalysts (SACs) with metal–nitrogen (M–N) sites are one of the most promising electrocatalysts for electrochemical carbon dioxide reduction (ECO$_2$R). However, challenges in simultaneously enhancing the activity and selectivity greatly limit the efficiency of ECO$_2$R due to the improper interaction of reactants/intermediates on these catalytic sites. Herein, we report a carbon-based nickel (Ni) cluster catalyst containing both single-atom and cluster sites (NiNx-T, T = 500–800) through a ligand-mediated method and realize a highly active and selective electrocatalytic CO$_2$R process. The catalytic performance can be regulated by the dispersion of Ni–N species *via* controlling the pyrolysis condition. Benefitting from the synergistic effect of pyrrolic-nitrogen coordinated Ni single-atom and cluster sites, NiNx-600 exhibits a satisfying catalytic performance, including a high partial current density of 61.85 mA cm$^{-2}$ and a high turnover frequency (TOF) of 7,291 h$^{-1}$ at –1.2 V vs. RHE, and almost 100% selectivity toward carbon monoxide (CO) production, as well as good stability under 10 h of continuous electrolysis. This work discloses the significant role of regulating the coordination environment of the transition metal sites and the synergistic effect between the isolated single-site and cluster site in enhancing the ECO$_2$R performance.

Keywords: ligand-mediated, atomic dispersion, nickel clusters and single atoms, nickel-nitrogen catalytic sites, carbon dioxide reduction

## INTRODUCTION

Electrochemical carbon dioxide reduction (ECO$_2$R) of valuable fuel/chemicals, driven by renewable energy sources, offers a promising route to solve global warming and realize carbon neutrality (Shaikh et al., 2018; Sharifian et al., 2021). In particular, the produced high value-added chemicals/fuels can contribute to an industrial production-oriented carbon cycle and greatly alleviate the energy crisis (Kondratenko et al., 2013; Qiao et al., 2014). So far, a variety of catalysts (metal-free and metal-based catalysts, metal/covalent organic frameworks catalysts, etc.) have been widely developed to boost ECO$_2$R of the target products with high activity and selectivity in order to achieve a high conversion efficiency (Duan et al., 2017; Vasileff et al., 2018; Liu et al., 2018). Currently, noble metal catalysts, such as Au and Ag, have demonstrated a promising catalytic performance concerning the generated current density (>10 mA cm$^{-2}$) and Faradaic efficiency (>90%) for CO products, offering feasibility for CO$_2$ valorization (Ma et al., 2016; Wuttig et al., 2016). However, their high cost seriously limits further application of these noble metal catalysts in ECO$_2$R. To address these

challenges, exploring carbon-based metal–nitrogen (M–N) catalysts with atomically dispersed transition metal sites would be a compelling choice due to their low cost, tunable structure, considerable activity, good stability, etc. Moreover, their well-defined coordination environment facilitates the clarification of the active sites and catalytic mechanism, as well as deeper investigation of the local microenvironmental effects on the activity (Li Y et al., 2021; Chen et al., 2021; Lu et al., 2021).

Transitional M–N-based single-atom catalysts (SACs) have emerged as one of the novel class of carbon-based catalysts to replace the noble metal catalysts (Chen et al., 2021). This is because of their ability to largely facilitate the $ECO_2R$ process while inhibiting the competing hydrogen evolution reaction (HER) by the virtue of their unique electronic structure, tailorable structure, and maximum atom utilization (Yang Q et al., 2019). Given that $ECO_2R$ is a thermodynamically controlled reaction process, SACs equally encounter some inherent drawbacks that mainly limit their practical development. For example, Fe/Co SACs with uniform Fe-N/Co-N sites have an ultralow overpotential for converting $CO_2$ to CO. However, the product selectivity and current density of these catalysts at relatively high potentials will rapidly decrease due to the high energy barrier of CO desorption and the blockage of the active sites (Lin et al., 2019). In another case, despite a high CO selectivity, Ni SACs with Ni–N active sites often need a high overpotential to acquire considerable current density due to the weak adsorption of *COOH intermediates and thus low efficiency for the following *COOH intermediates generation (Ding et al., 2021). Therefore, it is imperative to develop SACs with optimized active centers that can exhibit a moderate interaction with each intermediate including *COOH and *CO toward promoting electrocatalytic $ECO_2R$ at low overpotential with high selectivity (Shi et al., 2014).

Herein, we develop atomically dispersed Ni-cluster catalysts with Ni–N coordination (NiNx-T, T = 500–800) through a ligand-mediated pyrolysis method. The resultant NiNx-T possesses well-defined isolated single-atom and sub-nanometer-sized cluster Ni sites with a pyrrolic-N coordination environment. By regulating the content of Ni-pyrrolic N and the dispersion of Ni species via controlling the pyrolysis condition, the $ECO_2R$ performance of NiNx-T can be optimized. The electrochemical characterizations show that NiNx-600 with optimized Ni-cluster exhibits higher catalytic activity than other contrast samples and Ni nanoparticles (Ni NPs), including a higher current density of 61.85 mA cm$^{-2}$, faster reaction rate with TOF of 7,291 h$^{-1}$, as well as more impressive selectivity of nearly 100% toward CO production. It also demonstrates a good stability over 10 h of continuous operation. This work highlights the significant role of regulating the coordination of transition metal sites and the synergistic effect between the isolated single-site and cluster site in enhancing the $ECO_2R$ performance.

# MATERIALS AND METHODS

## Chemicals

Nickel (II) acetate tetrahydrate [Ni $(Ac)_2 \cdot 4H_2O$, 99%] and 1,4,7,10-tetraazacyclododecane (cyclen, 97%) were purchased from Aladdin. XC-72R was purchased from SCI Materials

Hub. Ultrapure water was used in all experiments [Millipore, 18.2 MΩ·cm]. All chemical reagents were used as received without further purification.

## Synthesis of Carbon-Based Ni-Cluster Catalysts

In a typical synthesis, Ni $(Ac)_2 \cdot 4H_2O$ (8.5 mg) and cyclen (18.5 mg) were dissolved in 1.5 ml of water and then stirred for 1 h at ambient conditions to obtain the violet solution. Subsequently, 100 mg of the XC-72R carbon carrier was added to the solution and stirred for 6 h. The resulting mixture was freeze-dried at −60°C for 12 h to obtain the black powder. Next, the powder was transferred into a porcelain dish and heated at 600°C, under argon (Ar) atmosphere. After cooling down to room temperature, the product was washed with ultrapure water and ethanol several times and dried in an oven at 70°C for 12 h (named NiNx-600). Other samples were synthesized via a similar procedure, except changing the pyrolysis temperature (500, 700 and 800°C, named NiNx-500, NiNx-700, and NiNx-800).
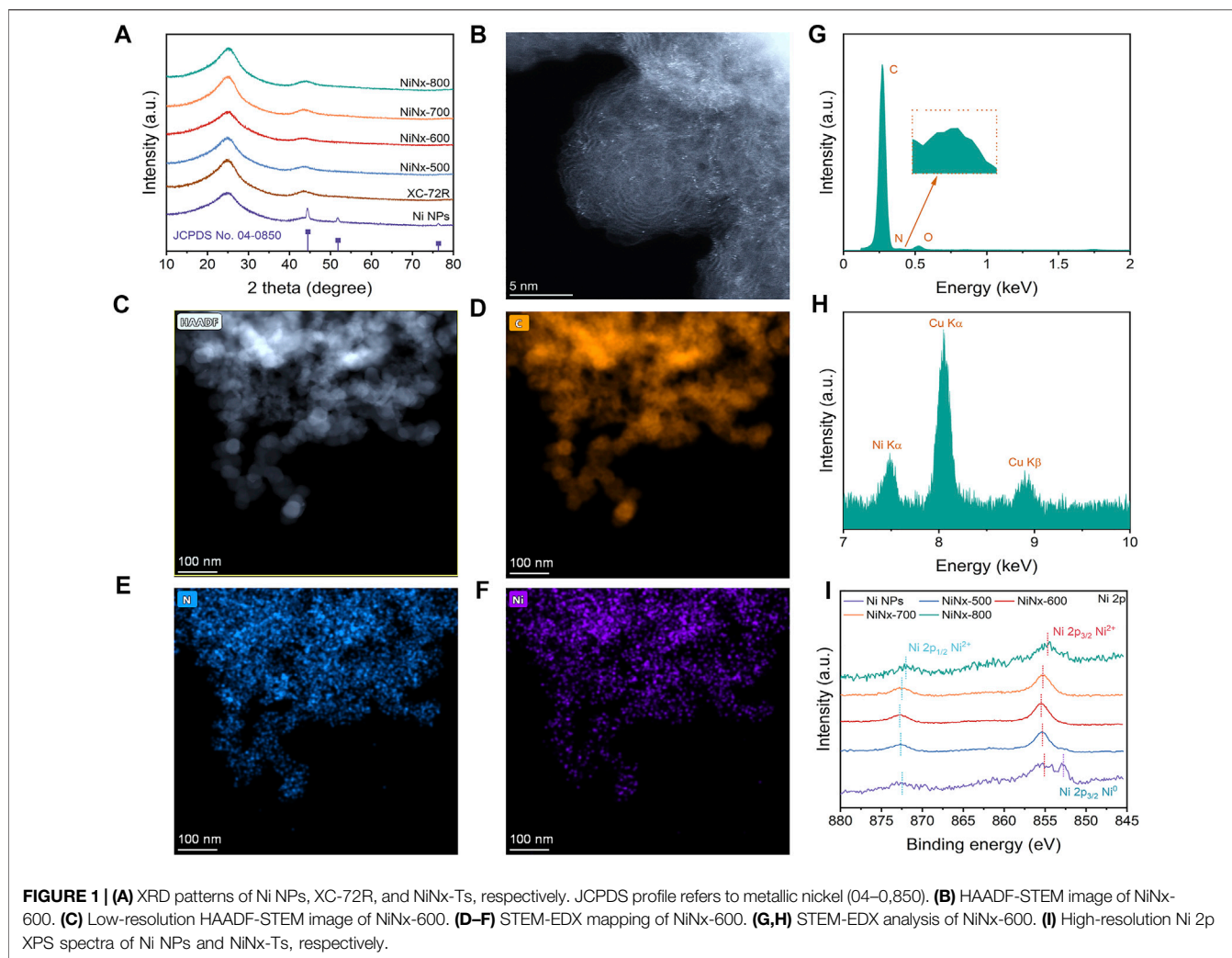
## Synthesis of Ni NPs

The Ni NPs were obtained via a similar method using NiNx-600, in addition to replacement of pyrolysis atmosphere (Ar) with 5% $H_2$/Ar.

## Characterizations

Powder X-ray diffraction (PXRD) patterns were collected using an X-ray diffractometer (Rigaku) with Cu Kα radiation (λ = 0.15406 nm). Scanning electron microscope (SEM) images were acquired from a Hitachi S4800 field emission electron microscope (10 kV). Transmission electron microscope images and corresponding energy-dispersive X-ray (EDX) elemental mapping were obtained using JEM-2100F and FEI Talos F200x electron microscopes (200 kV). High-angle annular dark-field STEM (HAADF-STEM) images were obtained from an FEI Themis Z STEM with double spherical aberration correctors working at 300 kV. Raman spectra were collected using a micro-Raman spectrometer (Renishaw). $N_2$ absorption/desorption isotherms were recorded on a Quantachrome Nova station. The X-ray photoelectron spectroscopy (XPS) analysis was carried out using a ThermoFisher Scientific ESCALAB 250Xi spectrometer. All spectra were calibrated according to the C 1s binding energy at 284.4 eV. The Ni loading of catalysts was conducted on an inductively coupled plasma-optical emission spectroscope (ICP-OES, PE Avio 200).

## Electrochemical Measurements

The evaluation of $ECO_2R$ performance was carried out in a classical three-electrode H-type system with a Nafion 212 film as separated component. An Ag/AgCl electrode was applied as a reference electrode and Pt mesh was used as a counter electrode. A carbon paper (Ce Tech Co. Ltd., N1S1007) was used as a working electrode. In a typical electrode preparation, the catalyst (5 mg) was dispersed in a mixed solution of ethanol (200 μL) and 0.5% Nafion solution (50 μL) by continuously sonicating for 1 h,

**FIGURE 1 | (A)** XRD patterns of Ni NPs, XC-72R, and NiNx-Ts, respectively. JCPDS profile refers to metallic nickel (04–0,850). **(B)** HAADF-STEM image of NiNx-600. **(C)** Low-resolution HAADF-STEM image of NiNx-600. **(D–F)** STEM-EDX mapping of NiNx-600. **(G,H)** STEM-EDX analysis of NiNx-600. **(I)** High-resolution Ni 2p XPS spectra of Ni NPs and NiNx-Ts, respectively.

and the dispersion liquid was drop-casted on a carbon paper with a certain catalyst loading of 0.5 mg cm$^{-2}$. The geometric surface area of the electrode was applied to calculate the current density. All the applied potentials were changed to a reversible hydrogen electrode (RHE) based on the following equation:

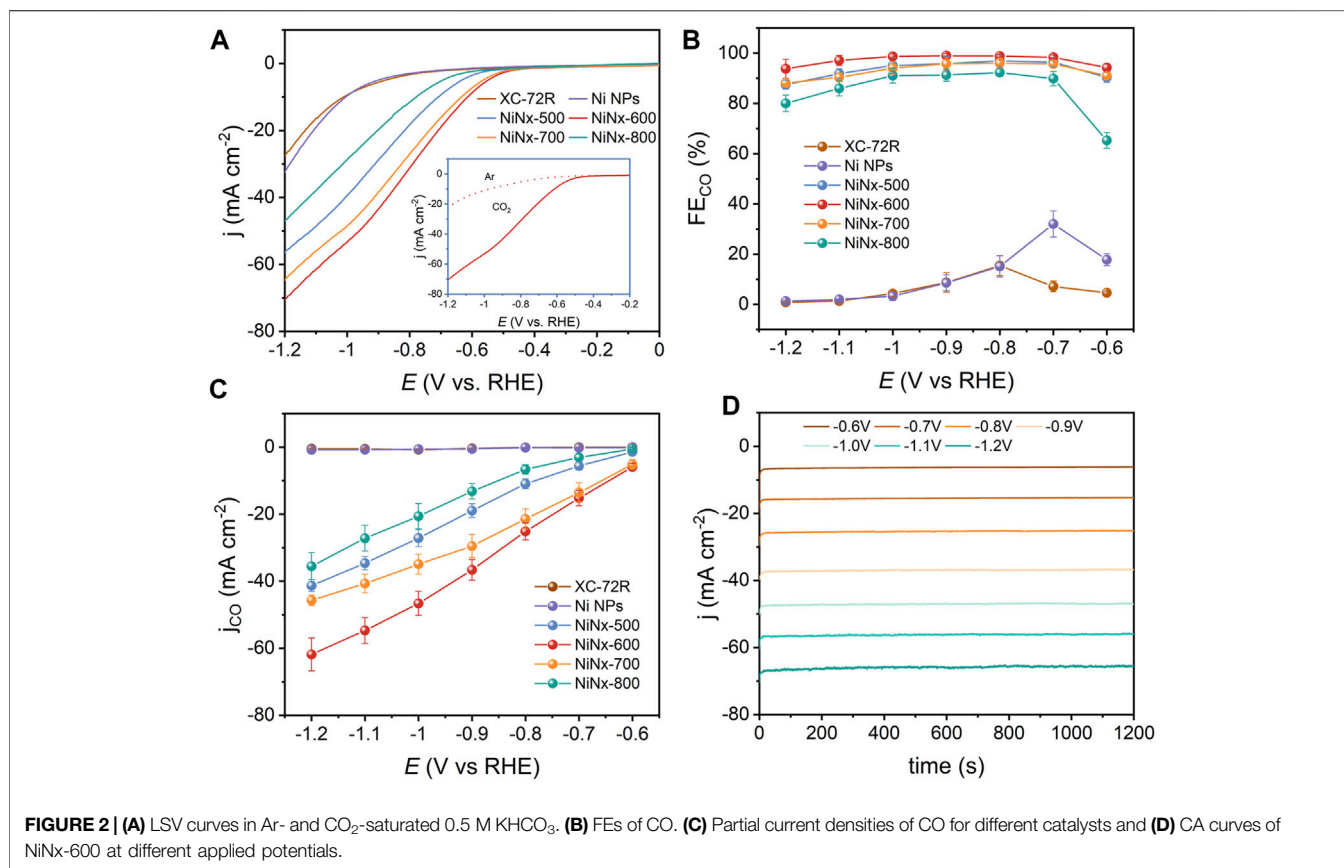$$E_{RHE} = E_{Ag/AgCl} + 0.05916 \times pH + 0.197 \quad (1)$$

Electrochemical measurements were processed on a Biologic VMP3 electrochemical workstation at ambient conditions. Linear sweep voltammetry (LSV) curves were acquired with a scan rate of 10 mV s$^{-1}$ in the Ar-and CO$_2$-saturated 0.5 M KHCO$_3$ solution. Electrochemical impedance spectroscopy (EIS) was carried out in the frequency range of 100 kHz to 0.1 Hz. For estimating the electrochemically active surface area, cyclic voltammetry (CV) curves were obtained from 20 to 120 mV s$^{-1}$ with an interval of 20 mV s$^{-1}$ at the potential range of 0.1–0.2 V vs. RHE. Chronoamperometry (CA) was measured at various potentials with a fixed time of 20 min, and the gas-phase components were detected *via* gas chromatography equipped with PDD and FID detectors (ThermoFisher

Scientific, Trace1300). High purity helium (99.9999%) and nitrogen (99.9999%) were employed as a carrier and make-up gas for chromatography, respectively. The liquid-phase products were analyzed using a Bruker NMR spectrometer (AVANCE-III HD 500). The FE of CO (FE$_{CO}$) and TOF were calculated *via* the following equations:

$$FE_{CO} = \frac{Q_{CO}}{Q_{Total}} = \frac{Z \times n \times F}{Q_{total}} \quad (2)$$

$$TOF = \frac{\frac{J_{product}}{nF}}{\frac{m_{cat \times \omega}}{M_{Ni}}} \quad (3)$$

where Q is the total charge transferred through the working electrode at different potentials, Z is the number of electrons transferred, which is 2 for both CO and H$_2$, n is the number of moles for a certain product, F is the Faradaic constant (96,485 C mol$^{-1}$), J$_{product}$ is the partial current density of a certain product, m$_{cat}$ is the catalyst loading, ω is the Ni content of the catalyst, and M$_{Ni}$ is the atomic mass of Ni (58.6934 g mol$^{-1}$).

**FIGURE 2 | (A)** LSV curves in Ar- and CO$_2$-saturated 0.5 M KHCO$_3$. **(B)** FEs of CO. **(C)** Partial current densities of CO for different catalysts and **(D)** CA curves of NiNx-600 at different applied potentials.
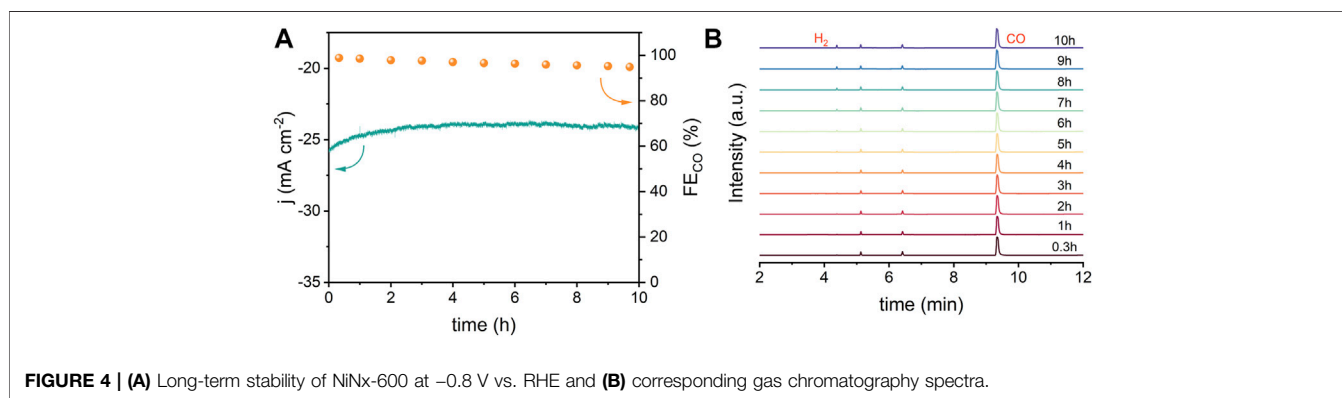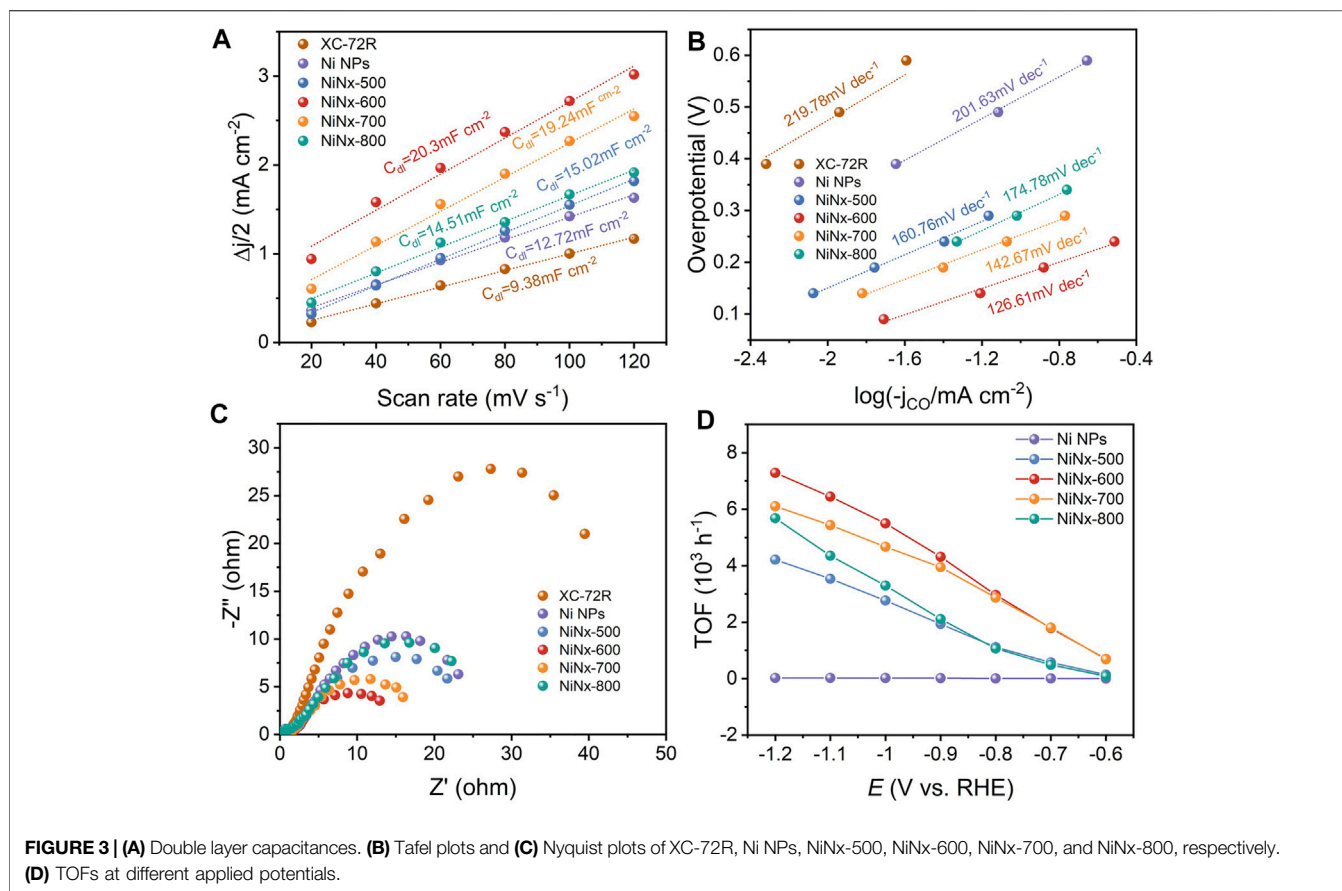
# RESULTS AND DISCUSSIONS

The synthesis process is shown in **Supplementary Figure S1**. In the process, through a ligand-mediated strategy, Ni ions could be coordinated with cyclen to form a Ni–cyclen complex and transformed to Ni–N species during pyrolysis. **Figure 1A** shows the PXRD patterns of the as-prepared catalysts, in which three diffraction peaks at 44.5°, 51.8°, and 76.4° were observed for Ni NPs, separately assigned to (111), (200), and (220) planes of crystalline Ni species (Ren et al., 2019). Only two broad graphitic peaks at 22.1° and 44.1° appear in the XRD patterns of NiNx-500 to NiNx-800 samples, which is similar to the XC-72R carrier and could be attributed to (002) and (100) planes of carbon (Yang H et al., 2019). The annular patterns in selected area electron diffraction (SAED) (**Supplementary Figures S2–S6**) further confirm the absence of crystalline Ni species (Zhang E et al., 2019). Moreover, none of the lattice stripes belonging to crystalline nickel species were detected in the high-resolution TEM (HRTEM) images of NiNx-500 to NiNx-800. These results all together confirm the amorphous state of Ni species on the carrier and verify the absence of Ni NPs for NiNx-T samples (Yan et al., 2018). On the contrary, the TEM and HRTEM images show the presence of Ni nanoparticles with a diameter of approximately 50 nm, accompanied with the exposed (111) plane (Fan et al., 2020), which is consistent with its XRD pattern (**Supplementary Figures S8A–D**). The corresponding EDX mapping of Ni NPs illustrates the dispersion of Ni and N

elements on the carbon carrier, suggesting the loading of N-doped Ni NPs on carbon substrate (**Supplementary Figures S8E–G**). The loading of Ni is 1.77, 0.60, 0.52, 0.46, and 0.13 wt.% for Ni NPs and NiNx-T, respectively, as indicated by the ICP-OES measurement (**Supplementary Table S2**). The decrease in the nickel species content is due to volatilization of metal species during high-temperature pyrolysis. To accurately verify the dispersion of Ni species in NiNx-500 to NiNx-800, HAADF-STEM measurements were carried out. As shown in **Figure 1B**, plenty of bright dots can be observed as isolated Ni single-atom and Ni clusters on the carrier for NiNx-600 (Wan et al., 2020). In addition, the relevant EDX elemental mapping and analysis (**Figures 1C–E**) disclose the homogeneous distribution of Ni, C, and N elements for NiNx-600, which illustrate the uniform dispersion of Ni species on the carbon carrier. Interestingly, when the temperature increases from 500 to 600°C, the dispersion of Ni atoms increases, and thus, the agglomeration of Ni species is reduced due to a thermal migration process. However, further increase in the temperature from 600 to 800°C results in a significant increase in the degree of agglomeration of Ni species owing to the unavoidable Ostwald ripening (**Supplementary Figures S9–S11**) (Wang et al., 2018). Therefore, the pyrolysis temperature plays a crucial role in controlling the dispersion of Ni species.

To investigate the surface area and pore structure, nitrogen adsorption and desorption isotherms were acquired at 77.3K. As shown in **Supplementary Figure S15**, the corresponding pore

**FIGURE 3 | (A)** Double layer capacitances. **(B)** Tafel plots and **(C)** Nyquist plots of XC-72R, Ni NPs, NiNx-500, NiNx-600, NiNx-700, and NiNx-800, respectively. **(D)** TOFs at different applied potentials.



**FIGURE 4 | (A)** Long-term stability of NiNx-600 at −0.8 V vs. RHE and **(B)** corresponding gas chromatography spectra.

size distributions show the presence of a mesoporous carbon skeleton for NiNx-T samples. It is thus clear that the carbon carrier has a good structural stability to ensure the sufficient exposure of abundant active sites during the catalytic process (Tan et al., 2018). In addition, compared with the XC-72R carbon carrier, the Brunauer–Emmett–Teller (BET) surface area of the NiNx-T samples (190.0, 142.0, 128.4, and 116.8 m² g⁻¹, respectively) loaded with Ni species is lower, which is attributed to the possible collapse of the pore structure during secondary pyrolysis and the import of Ni species with higher atomic mass than the C atom (Lin et al., 2019). Raman spectra in

**Supplementary Figure S14** show that the proportion of the D and G band ($I_D/I_G$; D: disorder, G: graphite) for NiNx-T is higher than that of the XC-72R carbon support, suggesting more local defects were introduced on the carbon carrier after secondary pyrolysis (Zhang E et al., 2019). Moreover, the amounts of defects for NiNx-T samples increase along with rising the pyrolysis temperature from 500 to 700°C. When pyrolyzed at 800°C, the $I_D/I_G$ value of NiNx-800 was reduced due to the increased degree of graphitization at higher temperatures. Thus, optimized pyrolysis conditions are beneficial for affording abundant pores and defects, facilitating the anchoring of Ni atoms

toward the uniform dispersion of Ni species, which is favorable for sufficient mass/electron transfer during the catalytic process.

To investigate the chemical state and coordination environment, the X-ray photoelectron spectroscopy (XPS) technique was implemented. The high-resolution Ni 2p XPS spectrum (**Figure 1I**) of Ni NPs exhibit three peaks at 852.8, 855.5, and 873.1 eV, respectively, which are ascribed to Ni $2p_{3/2}$ $Ni^0$, Ni $2p_{3/2}$ $Ni^{2+}$, and Ni $2p_{1/2}$ $Ni^{2+}$, respectively, indicating that the average chemical state of the nickel species in Ni NPs is between 0 and +2 (Feng et al., 2021). Unlike Ni NPs, no peaks attributed to Ni$2p_{3/2}$ $Ni^0$ appears in the high-resolution Ni 2p XPS spectra of NiNx-500 to NiNx-700. Only two peaks, which belong to Ni $2p_{3/2}$ $Ni^{2+}$ and Ni $2p_{1/2}$ $Ni^{2+}$, appear at binding energy at 852.8 and 873.1 eV, respectively. The higher binding energy of Ni $2p_{3/2}$ $Ni^{2+}$ in the NiNx-600 samples reveal the higher oxidation state of Ni species compared to that in other NiNx-T samples (Jia et al., 2021). This is due to the increased concentration of dispersed Ni–N species along with the reduced amounts of Ni clusters by the optimization in metal dispersion, which is consistent with the aforementioned HAADF-STEM results. The high-resolution C 1s spectra can be deconvoluted into four peaks located at 284.4, 286.2, 289.04, and 290.86 eV, respectively (**Supplementary Figure S12**), which are attributed to C=C, C-O/C-N, C=O, and the satellite peak of C 1s, respectively (Hou et al., 2019). The high-resolution N 1 s spectra of the samples indicate the presence of pyridinic N (398.1 eV), pyrrolic N (399.3 eV), graphitic N (400.5 eV), and quaternary N (401.37 eV) species (**Supplementary Figure S13**) for NiNx-T samples (Cheng et al., 2018). Notably, apart from Ni NPs, the peak at 398.8 eV attributed to Ni–N coordination was observed for NiNx-T samples, stemming from the pyrolytic Ni–cyclen complex precursors, in which Ni was coordinated to N atoms in a five-membered ring. Moreover, the higher amount of pyrrolic N species than pyridinic N moieties also implies that most of the Ni atoms on the carrier are coordinated with pyrrolic N instead of pyridinic N (Li J et al., 2021). NiNx-600 has an optimized Ni–N content, outperforming other samples. The content of Ni–N species shows a volcanic trend when increasing the pyrolysis temperature and reaches a maximum value at 600°C, suggesting that Ni atoms are gradually coordinating with N and resulting in the atomic dispersion of the Ni site at higher temperatures.

The evaluation of ECO$_2$R activities of XC-72R, Ni NPs, and NiNx-Ts were measured in a typical three-electrode H-type cell containing a 0.5 M KHCO$_3$ electrolyte (**Supplementary Figure S16**). As shown by LSV curves in **Figure 2A**, NiNx-600 exhibits a higher current density and lower onset potential in CO$_2$-saturated electrolyte from −0.5 to −1.2 V vs. RHE, which observably exceeds with those of the other five samples. Moreover, for NiNx-600, the current density significantly decreases and the onset potential raises when the electrolyte is changed from CO$_2$-saturated to Ar-saturated solution, which suggests its superiority for ECO$_2$R to the competitive HER process and manifests that the boosted activity of NiNx-600 originates from CO$_2$ reduction (Zhang H et al., 2019). Chronoamperometry (CA) was used to evaluate the total current density. Meanwhile, the gas products were detected by online GC (**Figure 4B**), and the liquid products

were analyzed by offline 1H NMR (**Supplementary Figure S19**). The results indicate that only H$_2$ and CO are detected for the synthesized samples during the ECO$_2$R process. **Figure 2B** and **Supplementary Figure S17** demonstrate the CA curves from −0.6 to −1.2 V vs. RHE. NiNx-600 holds the highest total current density with current densities of −6.25 mA cm$^{-2}$ at −0.6 V vs. RHE and −65.93 mA cm$^{-2}$ at −1.2 V vs. RHE, surpassing those of NiNx-500 (−1.58 and −47.24 mA cm$^{-2}$), NiNx-700 (−5.65 and −51.83 mA cm$^{-2}$), and NiNx-800 (−0.87 and −44.38 mA cm$^{-2}$). The higher current density of NiNx-600 with less Ni loading than NiNx-500 and Ni NPs suggest the important role of atomically dispersed Ni catalysts in promoting ECO$_2$R. Although XC-72R and Ni NPs are able to achieve a high total current density, they have a very low CO selectivity with a maximum FE$_{CO}$ of about 20% at the potential range of −0.6 V to −1.2 V vs. RHE (**Figure 2B**) due to the lack of effective active sites for selective CO$_2$RR over HER. Moreover, NiNx-600 demonstrates a higher selectivity than other samples over the entire potential range, with a maximum FE$_{CO}$ of 99%, which is among the best electrocatalysts for ECO$_2$R to CO (**Supplementary Table S3**). **Figure 2D** shows the potential-determined CO partial current density (j$_{CO}$). NiNx-600 achieves a j$_{CO}$ of 5.89 mA cm$^{-2}$ at −0.6 V vs. RHE, which is 512- and 78-fold higher than that of XC-72R and Ni NPs, respectively, verifying that the catalytic activity of NiNx-600 originates from plenty of atomically dispersed and pyrrolic N-coordinated Ni species.

The electrochemical active surface (ECSA) was evaluated from double-layer capacitance (C$_{dl}$) to clarify the source of the excellent catalytic performance of Ni–N sites. As shown in **Figure 3A** and **Supplementary Figure S18**, NiNx-600 achieves a substantial C$_{dl}$ of 20.3 mF cm$^{-2}$ and thus a higher ECSA than other NiNx-T samples, Ni particles and XC-72R carbon, which is beneficial to expose more active sites for enhancing the ECO$_2$R performance (Duan et al., 2018). Tafel plots were carried out to reveal the reaction kinetics on different active sites (**Figure 3B**). Tafel slopes of 219.78, 201.63, 160.76, 174.78,142.67, and 126.61 mV dec$^{-1}$ were fitted for XC-72R, Ni NPs, NiNx-500, NiNx-800, NiNx-700, and NiNx-600, respectively. These results reveal that the rate-determining step of ECO$_2$R on Ni–N sites for NiNx-600 is the proton-coupled electron transfer step to form the *COOH intermediate (Kong et al., 2021) as its Tafel slope is close to 118 mV dec$^{-1}$. Notably, the markedly lower Tafel slope of NiNx-600 indicates enhanced reaction kinetics in the ECO$_2$R process compared to the other counterparts (Duan et al., 2021). The Nyquist plots were acquired from electrochemical impedance spectroscopy (EIS) measurements. NiNx-T samples exhibit a lower charge transfer resistance compared to the bare XR-72R carbon carrier and Ni NPs, implying the highly dispersed Ni species on the carbon carriers favor a faster electron transfer kinetics than bulk Ni particles (**Figure 3C**). Among NiNx-T samples, NiNx-600 shows the lowest impedance, which originates from the promoted electron transfer kinetics by the higher content of atomic dispersed Ni species and the uniformly dispersed nickel species on the carbon carrier (**Figure 1B** and **Supplementary Figures S9–S11**). These all together endow NiNx-600 with an outperforming ECO$_2$R activity than other contrast catalysts. The

intrinsic activity of Ni-containing catalysts was uncovered by calculating the turnover frequency (TOF). The calculated TOFs at $-1.2$ V vs. RHE for Ni NPs and NiNx-Ts are 26, 4,217, 7,291, 6,106, and 5,686 $h^{-1}$, respectively. The highest TOF for NiNx-600 suggests the atomic Ni–N sites, and the dominance of single-atom combined with cluster sites greatly contribute to the highly boosted activity in $ECO_2R$ (**Figure 3D**). The stability of NiNx-600 during long-term electrocatalysis is shown in **Figure 4**. The total current density exhibits a negligible attenuation and its $FE_{CO}$ maintains 96% of the initial FE, manifesting the good stability of Ni–N sites in NiNx-600 in electrocatalytic $ECO_2R$. The comparison of XRD patterns, Raman spectra, and high-resolution Ni 2p XPS spectra for NiNx-600 before and after 10 h electrolysis also manifests the structure and chemical state of the carbon carrier and Ni species (**Supplementary Figures S20A–C**). The HAADF-STEM image in **Supplementary Figure S20** indicates the absence of the formation of bulk Ni species during the catalytic process and the maintenance of the atomic-level dispersion. During the $ECO_2R$ process, the valence state of the Ni active center decreases because electrons in the catalyst are transferred to the reactants and intermediates. The performance comparison of NiNx-600 and other single-atom catalysts further highlights the superiority of the ensemble of single atoms and clusters in boosting the high-efficiency $ECO_2R$ process (**Supplementary Table S3**).

## CONCLUSION

In summary, we have synthesized a series of atomically dispersed Ni single-atom and cluster catalysts for boosting $ECO_2R$ to CO by importing the pyrrolic N-coordinated Ni species on the carbon carrier. Upon modulation of the dispersion of Ni species and the content of pyrrolic N moieties through temperature control, NiNx-600 with well-dispersed Ni-pyrrolic N single-atom and cluster sites demonstrates a considerable electrocatalytic $ECO_2R$ performance with a maximum $j_{CO}$ of 61.85 mA $cm^{-2}$ and corresponding highest $FE_{CO}$ of 99%, as well as excellent TOF of 7,291 $h^{-1}$. The contrast results indicate that the integration of single atoms and clusters is greatly superior to single-atom catalysts in $ECO_2R$, wherein pyrrolic N-coordinated Ni species play an important role in promoting the $ECO_2R$ process for NiNx-600. This work highlights the significance of regulating the coordination of transition metal sites and the synergistic effect between the isolated single-site and cluster site in enhancing the $ECO_2R$ performance, which can be expanded to other complicated electrocatalysis such as nitrogen reduction, oxygen evolution, and nitrate reduction reaction.

## DATA AVAILABILITY STATEMENT

The raw data supporting the conclusion of this article will be made available by the authors, without undue reservation.

## AUTHOR CONTRIBUTIONS

H-XZ and QH co-conceived the idea and designed the experiments. QH conducted the experiments. D-XL performed the TEM and Raman measurements. RD contributed to HAADF-STEM measurements. QH and H-XZ co-wrote the manuscript. All the authors discussed the results and commented on the manuscript.

## FUNDING

## ACKNOWLEDGMENTS

## SUPPLEMENTARY MATERIAL

The Supplementary Material for this article can be found online at: https://www.frontiersin.org/articles/10.3389/fchem.2021.837580/full#supplementary-material

## REFERENCES

Chen, J., Li, Z., Wang, X., Sang, X., Zheng, S., Liu, S., et al. (2021). Promoting CO 2 Electroreduction Kinetics on Atomically Dispersed Monovalent Zn I Sites by Rationally Engineering Proton-Feeding Centers. *Angew. Chem. Int. Ed.* 60, 2–12. doi:10.1002/anie.202111683

Cheng, Y., Zhao, S., Johannessen, B., Veder, J. P., Saunders, M., Rowles, M. R., et al. (2018). Atomically Dispersed Transition Metals on Carbon Nanotubes with Ultrahigh Loading for Selective Electrochemical Carbon Dioxide Reduction. *Adv. Mater.* 30, 1706287. doi:10.1002/adma.201706287

Ding, T., Liu, X., Tao, Z., Liu, T., Chen, T., Zhang, W., et al. (2021). Atomically Precise Dinuclear Site Active toward Electrocatalytic CO2 Reduction. *J. Am. Chem. Soc.* 143, 11317–11324. doi:10.1021/jacs.1c05754

Duan, X., Xu, J., Wei, Z., Ma, J., Guo, S., Wang, S., et al. (2017). Metal-Free Carbon Materials for CO 2 Electrochemical Reduction. *Adv. Mater.* 29, 1701784. doi:10.1002/adma.201701784

Duan, Y.-X., Meng, F.-L., Liu, K.-H., Yi, S.-S., Li, S.-J., Yan, J.-M., et al. (2018). Amorphizing of Cu Nanoparticles toward Highly Efficient and Robust Electrocatalyst for CO2 Reduction to Liquid Fuels with High Faradaic Efficiencies. *Adv. Mater.* 30, 1706194. doi:10.1002/adma.201706194

Duan, Y. X., Zhou, Y. T., Yu, Z., Liu, D. X., Wen, Z., Yan, J. M., et al. (2021). Boosting Production of HCOOH from CO 2 Electroreduction via Bi/CeO X. *Angew. Chem. Int. Ed.* 60, 8798–8802. doi:10.1002/anie.202015713

Fan, Q., Hou, P., Choi, C., Wu, T. S., Hong, S., Li, F., et al. (2020). Activation of Ni Particles into Single Ni-N Atoms for Efficient Electrochemical Reduction of CO 2. *Adv. Energ. Mater.* 10, 1903068. doi:10.1002/aenm.201903068

Feng, Y., Long, S., Chen, B., Jia, W., Xie, S., Sun, Y., et al. (2021). Inducing Electron Dissipation of Pyridinic N Enabled by Single Ni-N4 Sites for the Reduction of Aldehydes/Ketones with Ethanol. *ACS Catal.* 11, 6398–6405. doi:10.1021/acscatal.1c01386

Hou, Y., Qiu, M., Kim, M. G., Liu, P., Nam, G., Zhang, T., et al. (2019). Atomically Dispersed Nickel-Nitrogen-Sulfur Species Anchored on Porous Carbon Nanosheets for Efficient Water Oxidation. *Nat. Commun.* 10, 1392. doi:10.1038/s41467-019-09394-5

Jia, C., Li, S., Zhao, Y., Hocking, R. K., Ren, W., Chen, X., et al. (2021). Nitrogen Vacancy Induced Coordinative Reconstruction of Single-Atom Ni Catalyst for Efficient Electrochemical CO 2 Reduction. *Adv. Funct. Mater.* 31, 2107072. doi:10.1002/adfm.202107072

Kondratenko, E. V., Mul, G., Baltrusaitis, J., Larrazábal, G. O., and Pérez-Ramírez, J. (2013). Status and Perspectives of CO2 Conversion into Fuels and Chemicals by Catalytic, Photocatalytic and Electrocatalytic Processes. *Energy Environ. Sci.* 6, 3112–3135. doi:10.1039/C3EE41272E

Kong, X., Ke, J., Wang, Z., Liu, Y., Wang, Y., Zhou, W., et al. (2021). Co-based Molecular Catalysts for Efficient CO2 Reduction via Regulating Spin States. *Appl. Catal. B Environ.* 290, 120067. doi:10.1016/j.apcatb.2021.120067

Li J, J., Jiang, Y.-f., Wang, Q., Xu, C.-Q., Wu, D., Banis, M. N., et al. (2021). A General Strategy for Preparing Pyrrolic-N4 Type Single-Atom Catalysts via Pre-located Isolated Atoms. *Nat. Commun.* 12, 6806. doi:10.1038/s41467-021-27143-5

Li Y, Y., Zhang, S. L., Cheng, W., Chen, Y., Luan, D., Gao, S., et al. (2021). Loading Single-Ni Atoms on Assembled Hollow N-Rich Carbon Plates for Efficient CO 2 Electroreduction. *Adv. Mater.* 34, 2105204. doi:10.1002/adma.202105204

Lin, L., Li, H., Yan, C., Li, H., Si, R., Li, M., et al. (2019). Synergistic Catalysis over Iron-Nitrogen Sites Anchored with Cobalt Phthalocyanine for Efficient CO 2 Electroreduction. *Adv. Mater.* 31, 1903470. doi:10.1002/adma.201903470

Liu, H., Chu, J., Yin, Z., Cai, X., Zhuang, L., and Deng, H. (2018). Covalent Organic Frameworks Linked by Amine Bonding for Concerted Electrochemical Reduction of CO2. *Chem* 4, 1696–1709. doi:10.1016/j.chempr.2018.05.003

Lu, C., Jiang, K., Tranca, D., Wang, N., Zhu, H., Rodríguez-Hernández, F., et al. (2021). Electrochemical Reduction of Carbon Dioxide with Nearly 100 % Carbon Monoxide Faradaic Efficiency from Vacancy-Stabilized Single-Atom Active Sites. *J. Mater. Chem. A.* 44, 24955–24962. doi:10.1039/D1TA05990D

Ma, M., Trześniewski, B. J., Xie, J., and Smith, W. A. (2016). Selective and Efficient Reduction of Carbon Dioxide to Carbon Monoxide on Oxide-Derived Nanostructured Silver Electrocatalysts. *Angew. Chem. Int. Ed.* 55, 9748–9752. doi:10.1002/anie.201604654

Qiao, J., Liu, Y., Hong, F., and Zhang, J. (2014). A Review of Catalysts for the Electroreduction of Carbon Dioxide to Produce Low-Carbon Fuels. *Chem. Soc. Rev.* 43, 631–675. doi:10.1039/C3CS60323G

Ren, W., Tan, X., Yang, W., Jia, C., Xu, S., Wang, K., et al. (2019). Isolated Diatomic Ni-Fe Metal-Nitrogen Sites for Synergistic Electroreduction of CO 2. *Angew. Chem. Int. Ed.* 58, 6972–6976. doi:10.1002/anie.201901575

Shaikh, R. R., Pornpraprom, S., and D'Elia, V. (2018). Catalytic Strategies for the Cycloaddition of Pure, Diluted, and Waste CO2 to Epoxides under Ambient Conditions. *ACS Catal.* 8, 419–450. doi:10.1021/acscatal.7b03580

Sharifian, R., Wagterveld, R. M., Digdaya, I. A., Xiang, C., and Vermaas, D. A. (2021). Electrochemical Carbon Dioxide Capture to Close the Carbon Cycle. *Energ. Environ. Sci.* 14, 781–814. doi:10.1039/D0EE03382K

Shi, C., Hansen, H. A., Lausche, A. C., and Nørskov, J. K. (2014). Trends in Electrochemical CO2 Reduction Activity for Open and Close-Packed Metal Surfaces. *Phys. Chem. Chem. Phys.* 16, 4720–4727. doi:10.1039/C3CP54822H

Tan, H., Tang, J., Zhou, X., Golberg, D., Bhatia, S. K., Sugahara, Y., et al. (2018). Preparation of 3D Open Ordered Mesoporous Carbon Single-Crystals and Their Structural Evolution during Ammonia Activation. *Chem. Commun.* 54, 9494–9497. doi:10.1039/C8CC05318A

Vasileff, A., Xu, C., Jiao, Y., Zheng, Y., and Qiao, S.-Z. (2018). Surface and Interface Engineering in Copper-Based Bimetallic Materials for Selective CO2 Electroreduction. *Chem* 4, 1809–1831. doi:10.1016/j.chempr.2018.05.001

Wan, J., Zhao, Z., Shang, H., Peng, B., Chen, W., Pei, J., et al. (2020). *In Situ* Phosphatizing of Triphenylphosphine Encapsulated within Metal-Organic Frameworks to Design Atomic Co1-P1n3 Interfacial Structure for Promoting Catalytic Performance. *J. Am. Chem. Soc.* 142, 8431–8439. doi:10.1021/jacs.0c02229

Wang, A., Li, J., and Zhang, T. (2018). Heterogeneous Single-Atom Catalysis. *Nat. Rev. Chem.* 2, 65–81. doi:10.1038/s41570-018-0010-1

Wuttig, A., Yaguchi, M., Motobayashi, K., Osawa, M., and Surendranath, Y. (2016). Inhibited Proton Transfer Enhances Au-Catalyzed CO2-to-fuels Selectivity. *Proc. Natl. Acad. Sci. USA* 113, E4585–E4593. doi:10.1073/pnas.1602984113

Yan, C., Li, H., Ye, Y., Wu, H., Cai, F., Si, R., et al. (2018). Coordinatively Unsaturated Nickel-Nitrogen Sites towards Selective and High-Rate CO2electroreduction. *Energ. Environ. Sci.* 11, 1204–1210. doi:10.1039/C8EE00133B

Yang H, H., Wu, Y., Li, G., Lin, Q., Hu, Q., Zhang, Q., et al. (2019). Scalable Production of Efficient Single-Atom Copper Decorated Carbon Membranes for CO2 Electroreduction to Methanol. *J. Am. Chem. Soc.* 141, 12717–12723. doi:10.1021/jacs.9b04907

Yang Q, Q., Yang, C.-C., Lin, C.-H., and Jiang, H.-L. (2019). Metal-Organic-Framework-Derived Hollow N-Doped Porous Carbon with Ultrahigh Concentrations of Single Zn Atoms for Efficient Carbon Dioxide Conversion. *Angew. Chem. Int. Ed.* 58, 3511–3515. doi:10.1002/anie.201813494

Zhang E, E., Wang, T., Yu, K., Liu, J., Chen, W., Li, A., et al. (2019). Bismuth Single Atoms Resulting from Transformation of Metal-Organic Frameworks and Their Use as Electrocatalysts for CO2 Reduction. *J. Am. Chem. Soc.* 141, 16569–16573. doi:10.1021/jacs.9b08259

Zhang H, H., Li, J., Xi, S., Du, Y., Hai, X., Wang, J., et al. (2019). A Graphene-Supported Single-Atom FeN 5 Catalytic Site for Efficient Electrochemical CO 2 Reduction. *Angew. Chem. Int. Ed.* 58, 14871–14876. doi:10.1002/anie.201906079